Materials Advances

ROYAL SOCIETY OF CHEMISTRY

PAPER

View Article Online
View Journal | View Issue

Cite this: *Mater. Adv.*, 2025, 6, 8645

Antibacterial nitrogen-containing mesostructured SBA-15-type materials: insight into functional groups and surface polarity

Mohamed Amine Benzaouia,[a] Othmane Dardari,[a] Ghanem Hamdoun,[a] Nadia Katir [a] and Abdelkrim El Kadib *[ab]

Received 6th July 2025,
Accepted 8th October 2025

DOI: 10.1039/d5ma00714c

rsc.li/materials-advances

Several nitrogen-containing organofunctionalized SBA-15-type materials have been successfully prepared and characterized. Besides the well-known aminopropyl-modified silica, propyl-dimethyl-octadecyl-ammonium and propyl-pyridyl-pyridinium have also been used for tethering the framework through Pluronic-templated sol–gel hydrolysis and co-condensation. Regardless of the nature of the starting precursors, their functionalities and/or their bulkiness, well-ordered silica mesostructures with high surface areas, pore sizes and pore volumes were obtained, with the flexibility or rigidity fingerprint of the precursor being transcribed at the mesoscale. The accessibility to nitrogen functionalities has been assessed through adsorption of the anionic helianthine dye pollutant. Their antibacterial activity was next evaluated against Gram negative *Escherichia coli* and Gram positive *Staphylococcus aureus*, revealing primary dependence on the loading of ammonium and pyridinium groups and correlating well with their accessibility. A substantial increase in the antibacterial activity was noticed through trimethylsilylation of residual surface silanols, providing consequently an easy route towards more potent antibacterial materials, through switching surface polarity, without introducing any metal additive that could add cost and compromise their sustainability. We also demonstrate the utility of these nitrogen-containing solids to uptake and release pharmaceuticals, as exemplified by the entrapment of the well-established quercetin antioxidant, opening the way towards synergistic biomaterials.

Introduction

Since their discovery, nanostructured silica-based materials created through self-assembly and sol–gel polymerization have attracted significant attention.[1–5] Their high surface area, uniform pore size, versatile surface functionalization and excellent thermal stability render them ideal nanoreactors for various applications ranging from adsorption and catalysis to sensing and health.[6–9] In the realm of antibacterial materials, mesoporous silica serves not only as a host for bioactive silver, copper and gold nanoparticles and other alloys and mixed oxides, but also can be used as a carrier for conjugating metal-free ammonium-based antibacterial materials.[10–12] This option is largely preferred considering the detrimental effect of metal nanoparticles, including their side effects and toxicity for humans as well as their negative impact for the surrounding environment and the ecosystem.[13–15]

One of the fundamental assets of mesostructured SBA-15-type materials lies in their versatile surface chemistry associated with the presence of abundant surface silanols and the wealth of available precursors that are prone to react with them through stable siloxane bridges.[16–19] Surface functionalization of SBA-15 with nitrogen-containing groups is expected to provide potent antioxidant, antiviral and antibacterial materials,[7,20–24] as well as more sophisticated ceramic and three-dimensional bio-based nanostructures,[25–28] making it a valuable route to be explored towards advanced antimicrobial formulation and coating.[29] Yet, little is known regarding the structure–reactivity relationship of these immobilized systems compared to the non-immobilized ammonium functionalities.[30] Precedents in the literature have claimed that the hydrophobicity imparted by the grafted reagent prevents or at least minimize surface bacterial adhesion and hence the antibacterial resistive biofilm formation.[31–34] Unfortunately, the preparation of these rationally designed scaffolds is tedious and accounts heavily for the final cost of the antibacterial formulation.[35] Surprisingly, no reports have hitherto explored trivial silanol passivation near the antibacterial reagent to further repel contact by exacerbating surface hydrophobicity. We consequently set out to engage an in-depth study to gain further understanding on the precise effect that these functional groups can exert on the biological activity. With this aim, we have prepared a variety of modified SBA-15-type materials, the common thread being the presence

[a] *Euromed University of Fes, UEMF, Morocco. E-mail: a.elkadib@ueuromed.org*
[b] *Hassan II Academy of Science and Technology, Rabat, Morocco*

of nitrogen-containing groups (either amine or ammonium and aliphatic or aromatic) in the material framework. We further expanded the library of studied materials to their trimethylsilylated-surface congeners to unveil the possible role of the remaining surface silanols during the interaction of cells with the solid surface. We have also explored the entrapment of quercetin as a representative active pharmaceutical ingredient, opening indeed another channel towards synergistic drug transporters. Through accurate comparison, this study substantiates the importance of the accessibility to the functional group and further established a clear correlation between the outer-sphere surface polarity of the surface and its biological response.

Results and discussion

Synthesis and characterization of 1-(3-trimethoxysilylpropyl)-4-(4-pyridyl)pyridinium bromide

Besides the commercially available 3-aminopropyltriethoxysilane and 3-(trihydroxysilyl)propyldimethyloctadecyl ammonium (**NQSi**), we have also attempted to use another pyridinium-based cationic species for SBA-15 surface modification. For such a purpose, we have prepared 1-(3-trimethoxysilylpropyl)-4-(4-pyridyl)-pyridinium bromide through nucleophilic substitution attack of 4,4′-bipyridine towards iodopropyltrimethoxysilane at room temperature for 24 hours, followed by exchanging an iodide counter ion to bromide, for the reasons of solubility (Scheme 1). It should be noted that the direct use of bromopropyltrimethoxysilane against 4,4′-bipyridine failed probably because of the poor leaving ability of bromide compared to iodide. The targeted product (**PyrSi**) was isolated as an orange-colored powder in 90% yield and was spectroscopically characterized. Its FTIR, ^{1}H and ^{13}C NMR, and UV-vis analyses (Fig. S1–S3) were found to be comparable to those previously reported in the literature.[21,22]

Sol–gel mesoporous organosilica synthesis and characterization

Nitrogen-containing SBA-15-type organosilicas were prepared by co-condensing tetraethylorthosilicate (TEOS) as a silica source with a selected nitrogen-containing organomodifier (aminoproyltriethoxylsilane **APTES**, 1-(3-trimethoxysilylpropyl)-4-(4-pyridyl)pyridinium bromide **PyrSi** or 3-(trihydroxysilyl)propyl dimethyl octadecyl ammonium chloride **NQSi**), using the amphiphilic Pluronic P123 as a structure-directing agent (Fig. 1). Surfactant removal was then achieved through Soxhlet extraction using acidified ethanol.[36] The amount of the organosilane (**NQSi** or **PyrSi**) was varied to achieve either X = 1% or 5% grafting, as it will be denoted for each material (**SBA@NQ$^{X\%}$** and **SBA@Pyr$^{X\%}$**). Silica prepared using aminoproyltriethoxylsilane will be denoted as **SBA@NH$_2$$^{5\%}$**. Pristine silica SBA-15 was also prepared following the same procedure, using only TEOS as the silica source and will be denoted as **SBA@OH** to reflect the presence of residual silanols on its surface. Hexamethyldisilazane $(Me_3Si)_2NH$ was used as a trimethylsilylating agent towards the remaining surface silanols,[37] resulting in their transformation into hydrophobic trimethylsilyl groups. These surface passivated materials will be denoted as **SBA@NQ$^{X\%}$-SiMe$_3$** and **SBA@Pyr$^{X\%}$-SiMe$_3$**. They were used to comparatively elucidate the effect of the surface polarity on the biological response.

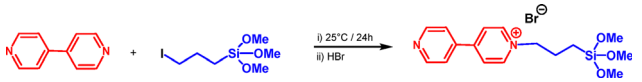

Scheme 1 Synthesis of the 1-(3-trimethoxysilylpropyl)-4-(4-pyridyl)-pyridinium bromide.

Fourier transform infrared (FTIR) spectroscopy of **SBA@NQ$^{X\%}$** and **SBA@Pyr$^{X\%}$** revealed a characteristic Si–O–Si peak at 1045 cm^{-1} (Fig. S4). At a lower organic loading of 1%, the Si–C band of the functionalizing agents could not be observed because of the marginal amount engaged in the initial solution. However, at 5% loading, such signature could be recognized at around 950 cm^{-1}, along with an increase in the intensity of the C–H bond. A further increase in the intensity of the Si–C band was noticed for trimethylsilylated **SBA@NQ$^{1\%}$-SiMe$_3$** and **SBA@Pyr$^{1\%}$-SiMe$_3$** materials, consistent with the introduction of additional methyl bridged to silicon groups.

Solid-state cross-polarization magic angle spinning nuclear magnetic resonance (CP-MAS^{29}Si NMR) shows the presence of high intensity peaks at −100 ppm and −109 ppm assigned, respectively, to Q^3 and Q^4 signals of the silica framework, while Q^2 seems to be minor and embedded within the shoulder of the fused Q^3 and Q^4 peaks. Besides, a weak T-type signal of the terminal silicon belonging to the linker could be recognized at −67 ppm for **SBA@Pyr$^{1\%}$** and was hardly observable at −74 ppm for **SBA@NQ$^{1\%}$**. However, the intensity of these T-type signals further increase at 5% loading and could be distinguished at −63 and −74 ppm for **SBA@NQ$^{5\%}$** and at −54 and −67 ppm for **SBA@Pyr$^{5\%}$** (Fig. 2a). This brings convincing evidence for the covalent bonding on the co-condensed silicon-containing **NQSi** and **PyrSi** precursors to the silica framework (Fig. 2). Solid-state CP MAS ^{13}C NMR of **SBA@NQ$^{5\%}$** confirmed the presence of an aliphatic skeleton (10 ppm to 68 ppm) of the **NQSi** chain (Fig. S5). Solid-state ^{1}H NMR of **SBA@Pyr$^{5\%}$** showed two broad signals around 10 ppm. The COSY experiment established a clear correlation between these signals, thereby confirming their attribution to the pyridine–pyridinium moieties incorporated into the mesoporous silica network (Fig. S6). In the trimethylsilylated **SBA@NQ$^{1\%}$-SiMe$_3$** and **SBA@Pyr$^{1\%}$-SiMe$_3$** materials, two trends have been observed: (i) the presence of intense signals at 13.26 and 13.65 ppm in solid-state CP-MAS ^{29}Si NMR spectra, unambiguously attributed to Si–O–$SiMe_3$; (ii) treatment of the surface causes more framework condensation as illustrated by the increased intensity of the Q^4-type signal at −109 ppm at the expense of the Q^3-type signal at −100 ppm (Fig. 2b).

Thermogravimetric analysis (TGA) reveals distinct behavior across different materials in terms of water evaporation and thermal stability, reflecting the difference imparted by the nature of nitrogen-containing organic groups (Fig. S7). All materials remove physisorbed water below 100 °C, with the water content being dependent on their organic functionalities.

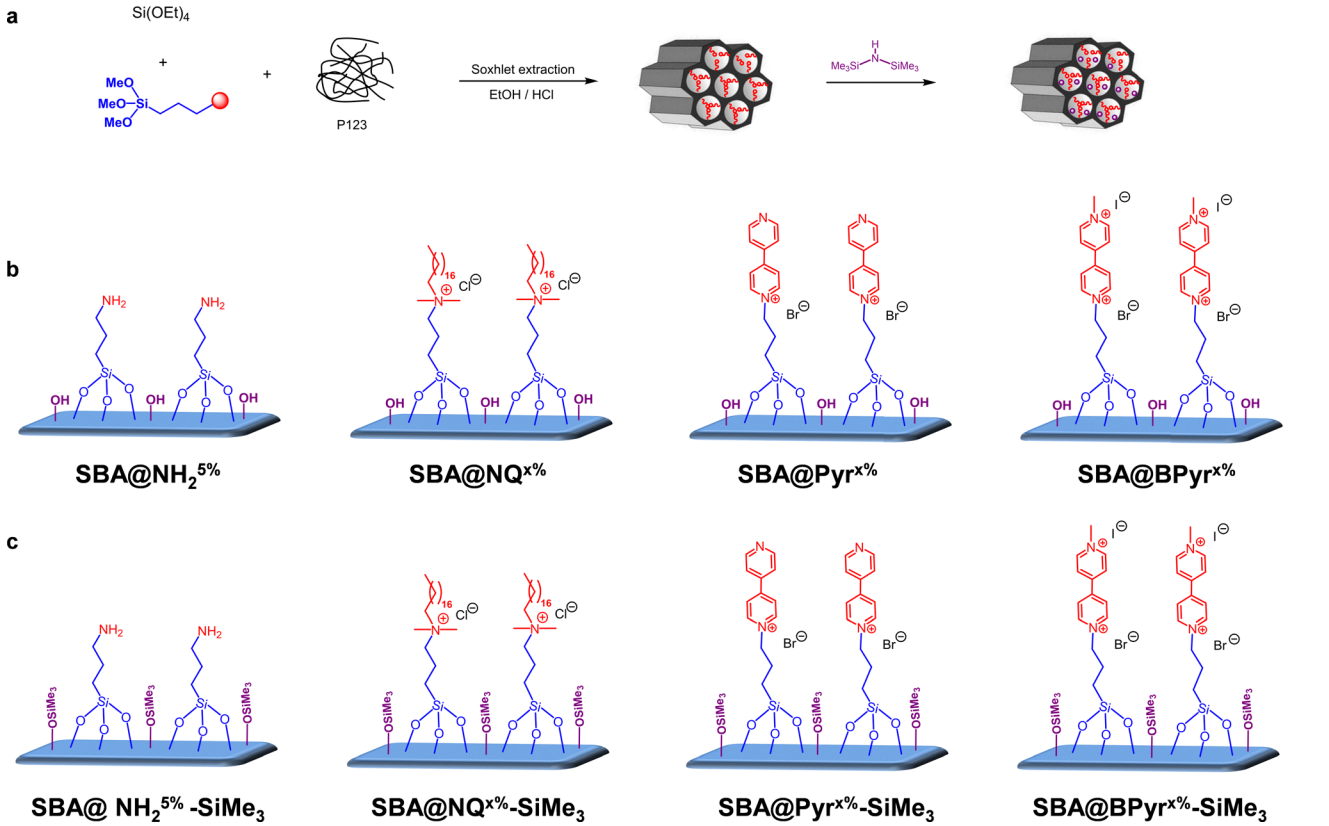

Fig. 1 (a) Multistep preparation of the SBA-15-type mesostructure involving the use of tetraethylorthosilicate (TEOS) and the co-condensing reagent as the silica source and the Pluronic as a template followed by Soxhlet extraction and surface passivation. (b) Chemical structure of the modified surface and the (c) passivated silica surface of each material after trimethylsilylation.

From 100 °C to 250 °C, organosilica materials maintain their stability, with no major changes observed up to 320 °C. Beyond this temperature, thermal degradation occurs, with **SBA@NQ$^{5\%}$** showing a more pronounced weight loss of 21%, compared to only 8% weight loss observed for **SBA@Pyr$^{5\%}$**. This discrepancy can be tentatively explained by the great thermal stability of aromatic derivatives compared to the aliphatic ones that are more prone to C–C oxidative scission at elevated temperatures.[38] Nitrogen elemental analysis further corroborates the presence of covalently linked nitrogen species that could normally leach out of the solution if only physisorbed (Table 1). The amount of nitrogen fits nearly the expected theoretical value, with an increase in its content (respectively by 4.1 and 4.27) with the increasing organic loading from 1% to 5% in **SBA@NQ$^{x\%}$** and **SBA@Pyr$^{x\%}$**. This means that nearly 85% of the engaged amount of the co-condensing reagent was assembled within the mesostructured framework during the early stage of the hydrolysis–condensation. The bulkiness of the **NQSi** reagent and its remarkably crowded nature did not hinder its quantitative grafting on the silica walls. This could be attributed to its hydrolysable $Si(OH)_3$ groups, known to react faster compared to conventional trialkoxysilyl groups that need an induction time for triggering hydrolysis and further condensation.

Nitrogen physisorption analysis shows an adsorption–desorption isotherm profile typical of SBA-15-type porous materials (Fig. 3 and Table 1). High surface areas of 745 $m^2\ g^{-1}$ for **SBA@NQ$^{1\%}$** and 666 $m^2\ g^{-1}$ for **SBA@Pyr$^{1\%}$** were obtained, being nearly comparable to the one of the pristine **SBA@OH** (720 $m^2\ g^{-1}$). The increased surface area of **SBA@NQ$^{1\%}$** and its expanded pore diameter to 6.4 nm, in spite of its bulkiness, suggests that the latter acts as a swelling reagent for the micellar medium.[39] For the two materials, increasing the amount of the co-condensing agent from 1% to 5% do not alter the mesostructure ordering but decreases the specific surface area from 745 to 515 $m^2\ g^{-1}$ for **SBA@NQ$^{5\%}$** and from 666 to 613 $m^2\ g^{-1}$ in the case of **SBA@Pyr$^{5\%}$**. More dramatic decrease in the specific surface area occurs upon surface trimethylsilylation, going down to 274 $m^2\ g^{-1}$ for **SBA@NQ$^{1\%}$-SiMe$_3$** and 365 $m^2\ g^{-1}$ for **SBA@Pyr$^{1\%}$-SiMe$_3$** (Fig. 3 and Fig. S8). This agrees with the quantitative surface trimethylsilyation evidenced by the great intensity of the corresponding signals at 13.26 and 13.65 ppm in solid-state ^{29}Si NMR. Consequently, bulkier trimethylsilyl groups are introduced to substitute discrete silanols, more plausibly at the pore entrance during the diffusion of the hydrophobic hexamethyldisilazane, thereby reducing the specific surface areas of the corresponding materials. A close look on the C_{BET} factor reveals a diverging pattern depending on the organic groups. C_{BET} has often taken as an indicator for the surface polarity of the solid surface, especially with regard to chemical functionalization.[39,40] Its decrease reflects a lower interaction with nitrogen, and hence a more inert and

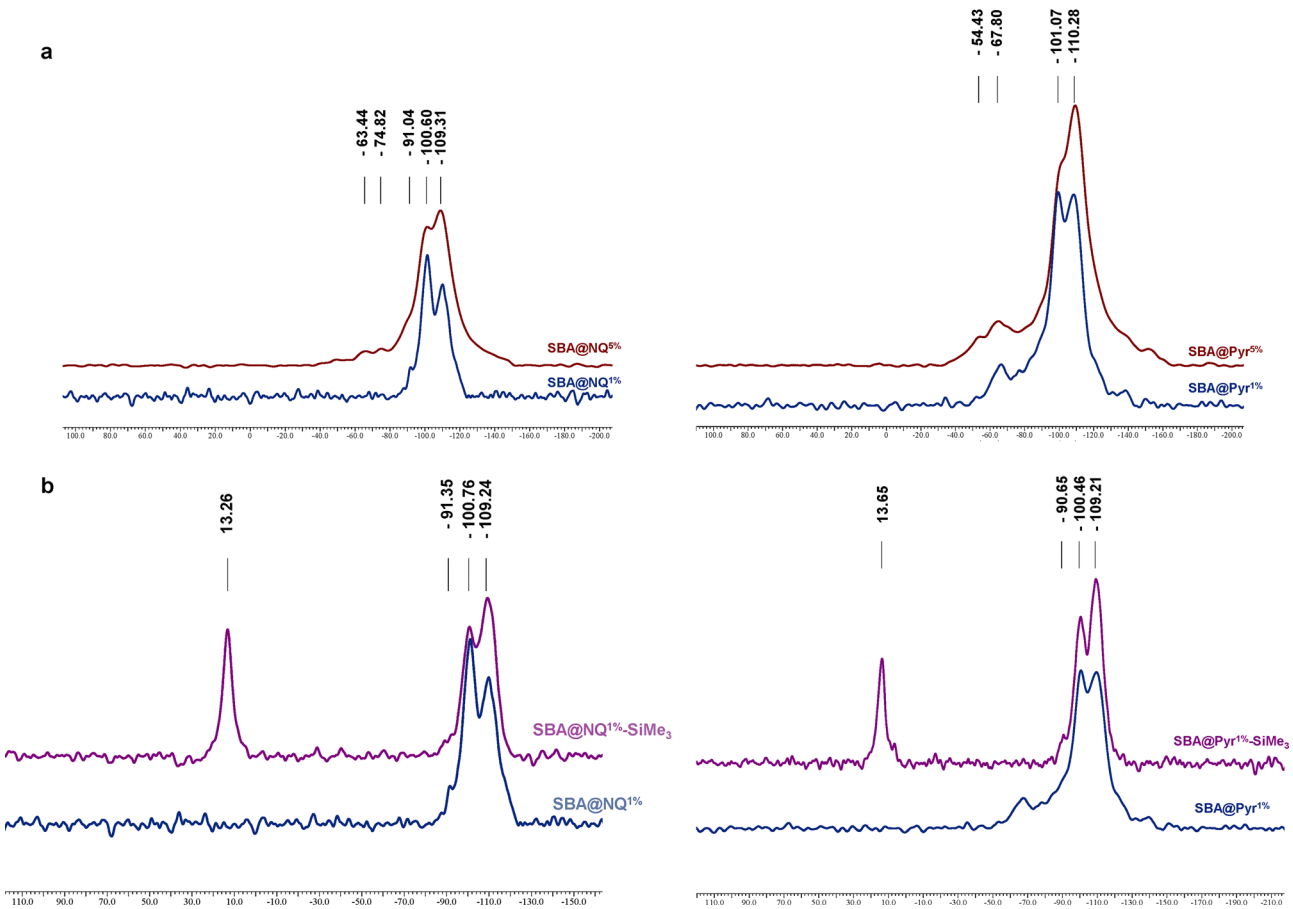

Fig. 2 Solid state NMR of nitrogen-containing SBA-15 materials. (a) ^{29}Si NMR of **SBA@NQ$^{1\%}$** *versus* **SBA@NQ$^{5\%}$** (left) and ^{29}Si NMR of **SBA@ Pyr$^{1\%}$** *versus* **SBA@ Pyr$^{5\%}$** (right). (b) ^{13}C NMR of **SBA@NQ$^{1\%}$** *versus* **SBA@NQ$^{1\%}$-SiMe$_3$** (left) and ^{13}C NMR of **SBA@Pyr$^{1\%}$** *versus* **SBA@Pyr$^{1\%}$-SiMe$_3$** (right).

Table 1 Textural properties and composition from nitrogen physisorption analysis, elemental analysis and thermogravimetric analysis

Materials	S_{area} (m^2 g^{-1})	D (nm)	V (cm^3 g^{-1})	C_{BET}	N (mmol g^{-1})	Grafting density (molecule nm^{-2})	% Residue at 600 °C
SBA@OH	720	5.6	0.8	140	—	—	81
SBA@NH$_2$$^{5\%}$	440	5.1	0.5	230	0.36	0.37	79
SBA@Pyr$^{1\%}$	666	5.9	0.7	253	0.11	0.05	78
SBA@Pyr$^{5\%}$	613	5	0.7	277	0.47	0.23	82
SBA@NQ$^{1\%}$	745	6.4	1	158	0.1	0.08	80
SBA@NQ$^{5\%}$	515	6	0.8	50	0.41	0.48	74
SBA@Pyr$^{1\%}$-SiMe$_3$	365	5.5	0.5	49	0.02	0.016	83
SBA@NQ$^{1\%}$-SiMe$_3$	274	5.9	0.5	36	0.028	0.061	68

hydrophobic solid surface. Native **SBA@OH** displays a C_{BET} value of 140. For **SBA@Pyr$^{1\%}$**, the recorded value of 253 indicates substantial surface polarity probably owing to the strong donating ability of the pyridine moieties, both as a hydrogen donor and an electron donor. Stronger interactions are further observed at 5% loading for **SBA@Pyr$^{5\%}$**, reflected by C_{BET} = 277 presumably because more polar pyridine–pyridinium groups are immobilized on the surface at the expense of surface silanols. In turn, **NQSi** coverage seems to impart the material surface increased hydrophobicity, consistent with the length of the octadecyl spacer. At 1% loading, no significant alteration occurs for **SBA@NQ$^{1\%}$** compared to the pristine **SBA@OH** (C_{BET} of 158 *versus* 140). At a lower loading of 1%, the grafting density of **NQSi** was equal to 0.08 molecule nm^{-1}, offering plausibly more empty and hence available space to interact with residual surface silanol groups. In contrast, a severe decrease to a C_{BET} value of 50 was observed for **SBA@NQ$^{5\%}$**, where we assume that at 5% loading, the surface was totally covered and hence becomes more hydrophobic. Incredibly, trimethylsilylated materials further decrease the C_{BET} values to 49 for **SBA@Pyr$^{1\%}$-SiMe$_3$** and 36 for **SBA@NQ$^{1\%}$-SiMe$_3$**, allowing us to draw two additional conclusions: (i) the highest polarity of **SBA@Pyr$^{X\%}$** does not only rely solely on the pyridine–pyridinium groups, but also in their proximal geometry and plausible interaction with surface silanols. The consumption of

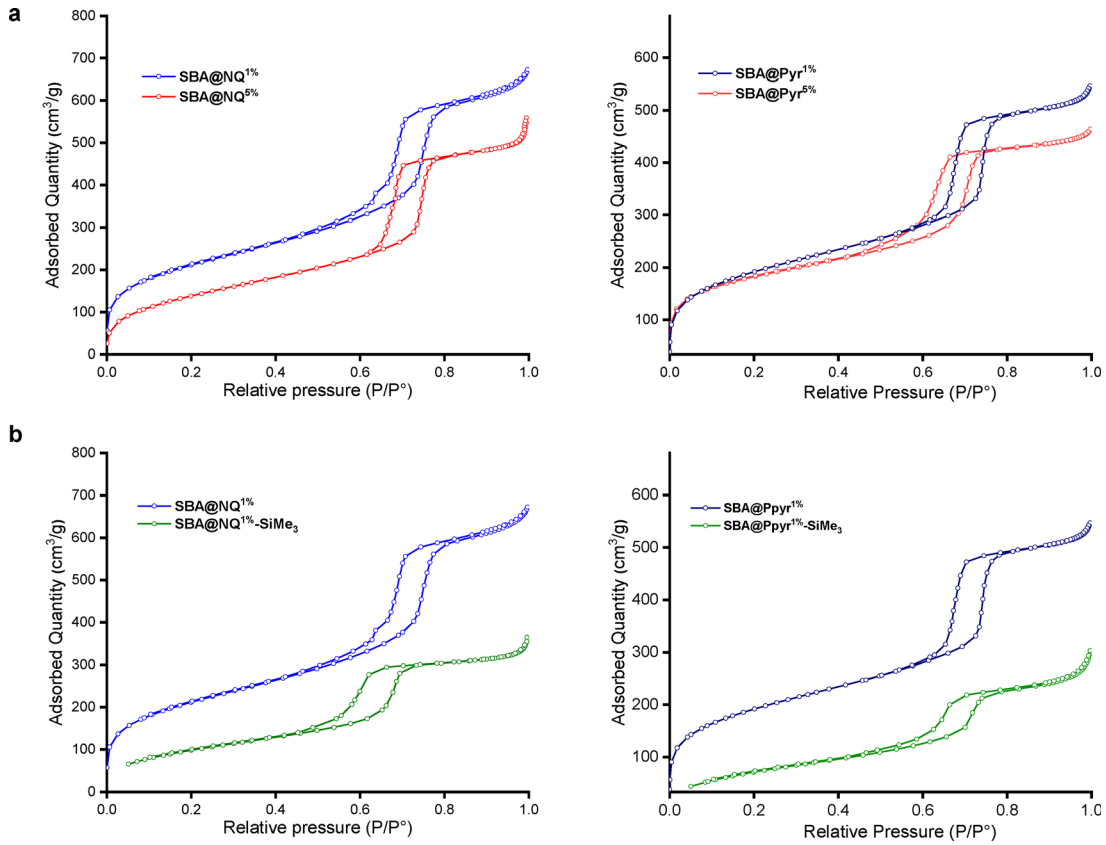

Fig. 3 Nitrogen adsorption–desorption isotherm profiles of nitrogen-containing SBA-15 materials. (a) **SBA@NQ$^{1\%}$** *versus* **SBA@NQ$^{5\%}$** (left) and **SBA@Pyr$^{1\%}$** *versus* **SBA@Pyr$^{5\%}$** (right). (b) **SBA@NQ$^{1\%}$** *versus* **SBA@NQ$^{1\%}$-SiMe$_3$** (left) and **SBA@Pyr$^{1\%}$** *versus* **SBA@Pyr$^{1\%}$-SiMe$_3$** (right).

these groups in **SBA@Pyr$^{X\%}$-SiMe$_3$** suppresses the stronger interaction previously seen for **SBA@Pyr$^{X\%}$**; (ii) trimethylsilylated **SBA@NQ$^{1\%}$-SiMe$_3$** behaves quite similarly to **SBA@NQ$^{5\%}$**. We in fact assume that, at high loading, **NQSi** distribution density along with the steric hindrance of the substituents at the nitrogen center hinders access to the exposed silanols, although they are still present on the surface. One might indeed conclude that the surface polarity of the corresponding materials could be tuned either by adjusting the loading of the tether or by trimethylsilylation.

Scanning electron microscopy (SEM) analysis allows visualization of the textured network at the microscale. Non-functionalized **SBA@OH** consists of uniform elongated aggregates with rod-like morphology, typical of Pluronic-templated mesoporous materials (Fig. S9). In the cases of **SBA@NQ$^{1\%}$** and **SBA@Pyr$^{1\%}$**, the images reveal rod-like structures, confirming the preservation of the mesostructured form of SBA-15 (Fig. 4). However, the way the rod-like structure aggregates to each other to build an extended secondary structure changes from one material to another. In the case of **SBA@NQ$^{1\%}$**, rods are twisted and this becomes more pronounced at 5% loading as it can be observed in the onset image (Fig. 4a). In contrast, those of **SBA@Pyr$^{1\%}$** linearly extend to form a more continuous rigid network. The resulting organization at the microscale can be attributed to the interplay of the used co-condensing reagent with the Pluronic and the nucleating siloxanes during the assembly of the mesostructure as it has already been reported for similar self-structuring precursors.[39,41] Transmission electron microscopy (TEM) images of the corresponding samples reveal well-defined nanoscale ordering, typical of the mesostructured silica network, with the dark regions corresponding to the dense silica walls, while the periodically arranged bright lines reflects the presence of uniform, ordered pores, in agreement with nitrogen sorption analysis. Besides, in the case of **SBA@NQ$^{1\%}$**, the twisted architecture could be easily recognized, further corroborating the original organization of the rods at the microscale. Such a twisted structure could not be seen in the case of **SBA@Pyr$^{1\%}$** where only direct anisotropic rods could be observed (Fig. 4b). In the whole, SEM and TEM images conclude that the co-condensing reagents used could be anchored on the silica framework with no detrimental effect on the pore uniformity or the regularity of the assembled network. Besides, the rigidity or flexibility fingerprint of the starting precursor transcribes in the hybrid at the microscale and even at the nanoscale.[42]

Accessibility test of functional groups

Given the complexity of the used **NQSi** and **PyrSi** precursors, a question arises concerning the accessibility of the corresponding cationic groups to the surrounding guests, including dyes and cells, once confined inside of the mesostructured framework. This accessibility is of prime importance regarding

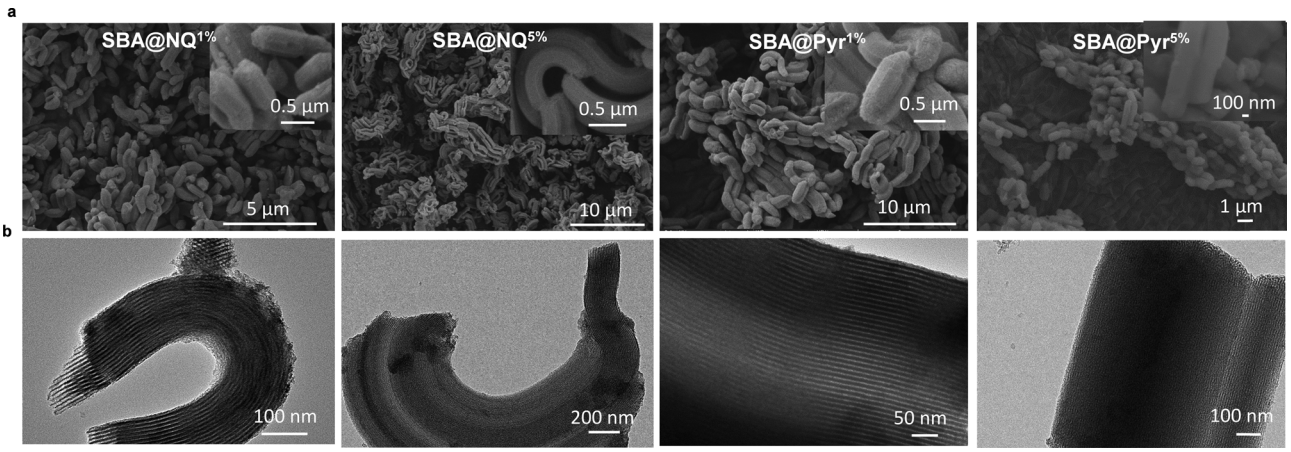

Fig. 4 SEM image (a) and TEM image (b) of, from left to right, **SBA@NQ$^{1\%}$**, **SBA@NQ$^{5\%}$**, **SBA@Pyr$^{1\%}$** and **SBA@Pyr$^{5\%}$**. Onset SEM images show twisted rods in the cases of **SBA@NQ$^{1\%}$** and of **SBA@NQ$^{5\%}$**, contrasting with more aligned rods in the cases of **SBA@Pyr$^{1\%}$** and **SBA@Pyr$^{5\%}$**.

their use as antibacterial and antiviral coating materials. We have indeed embarked to assess their adsorptive capacity for anionic dyes that could intuitively reflect the availability of the anchored functionalities inside of the mesopores. For such a purpose, we have selected helianthine (methyl orange) as a representative anionic dye.

At neutral pH of 6.5, unmodified silica **SBA@OH** failed to adsorb the anionic dye, recording less than 3% uptake, which exclude the involvement of the remaining silanols in interacting with the adsorbate. A significant uptake of 28% could be reached with **SBA@NH$_2$$^{5\%}$**, due to the possible hydrogen bonding with the primary amine groups. Surprisingly, a lower performance of 4% was recorded for **SBA@Pyr$^{5\%}$** because of the lower propensity of the exposed pyridine for hydrogen bonding. This lower uptake is also indicative of the inaccessibility to the cationic pyridinium fragment that seems to be buried inside the silica framework, and not exposed to be partnered with the anionic dye (Fig. 5). However, the uptake could be increased to 43% upon alkylation of the terminal pyridine through methylation to the bipyridinium decorating surface (denoted herein as **SBA@BPyr$^{5\%}$**). Although this post-modification induces severe reduction in the specific surface area (S_{BET} = 246 m^2 G^{-1}), transforming external pyridine groups into pyridinium provides the driving force for electrostatic interactions with the dye, allowing for its substantial removal from aqueous solution. Outstanding performance has been observed for **SBA@NQ$^{5\%}$**, reaching nearly fully removal (99%), which correspond to 16.7 mg g^{-1} of the dye. Interestingly, at a basic pH of 9.5, all the materials display poor adsorption ability, except **SBA@NQ$^{5\%}$**. The main reason for this decrease is probably the deprotonation occurring on the surface of these materials rendering them negatively charged, leading indeed to electrostatic repulsion with methyl orange (MO). The increased performance observed at an acidic pH of 2 for **SBA@OH**, **SBA@NH$_2$** and **SBA@Pyr$^{5\%}$** confirms our assumptions of the occurrence of adsorption through an ionic exchange mechanism. **SBA@NQ$^{5\%}$** maintains its highest adsorption capacity owing to the quaternary nature of its nitrogen center, hindering it from protonation or deprotonation and hence making it insensitive to pH variation. These experiments further demonstrate the full accessibility of the ammonium groups in **SBA@NQ$^{5\%}$** in spite of the presence of such lengthy dodecyl substituent that could hinder access to the nitrogen center. At an active site basis, the number of occupied nitrogen sites of **SBA@NQ$^{5\%}$** for adsorbing a methyl orange concentration of C_o = 10^{-4} mol L^{-1} was found to be 12.3%, meaning that a

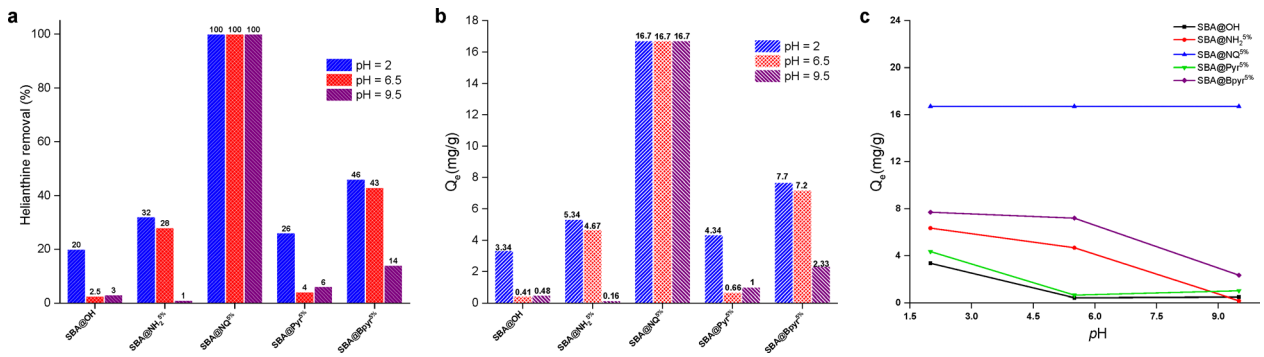

Fig. 5 Removal of helianthine (methyl orange) using silica and the modified silica surface; C_0 = 10^{-4} mol L^{-1}. (a) Percentage of helianthine removal, (b) adsorption capacity (Q_e, mg g^{-1}) and (c) overall effect of pH on the adsorption behavior of helianthine on organosilicas.

large portion of cationic groups is still available for interaction with the dye (Table S1). A further increase of the initial concentrations to 5.10^{-4} mol L^{-1} and 10^{-3} mol L^{-1} decreases the removal efficiency to 92% and 75%, respectively. This corresponds to maximum adsorption capacities of 75 mg g^{-1} and 123 mg g^{-1}, respectively (Fig. S10), meaning that 54% of the active nitrogen site are interacting for $C_0 = 5.10^{-4}$ mol L^{-1} and even 90% for a $C_0 = 10^{-3}$ mol L^{-1} (Table S1). This reflects the great exposure of the cationic site in **SBA@NQ$^{5\%}$**. Oppositely, one could also conclude on the inaccessibility of the pyridinium in **SBA@Pyr$^{5\%}$** that seems to be more oriented to the silica surface, probably through hydrogen bonding or week interactions with the neighboring surface silanols.

Antibacterial activity

Next, the antibacterial activity of these materials against *Escherichia coli* and *Staphylococcus aureus* was investigated. At the first glance, non-modified **SBA@OH** displays the lowest inhibitory effect, indicating that the pristine silica surface lacks appreciable antibacterial activity and consequently highlighting surface-functionalization as a key enabler to impart these materials with the requested bio-activity. More improvement was rather observed using both **SBA@NQ$^{X\%}$** and **SBA@Pyr$^{X\%}$**. In the case of *Staphylococcus aureus*, the former achieves inhibition zones of 5.9 and 8.4 mm at 1% and 5% loading, respectively. The latter achieves 7.4 and 9.7% mm, respectively, at 1% and 5% loading, outperforming indeed its aliphatic congeners (Fig. 6a and b). A similar trend was also observed

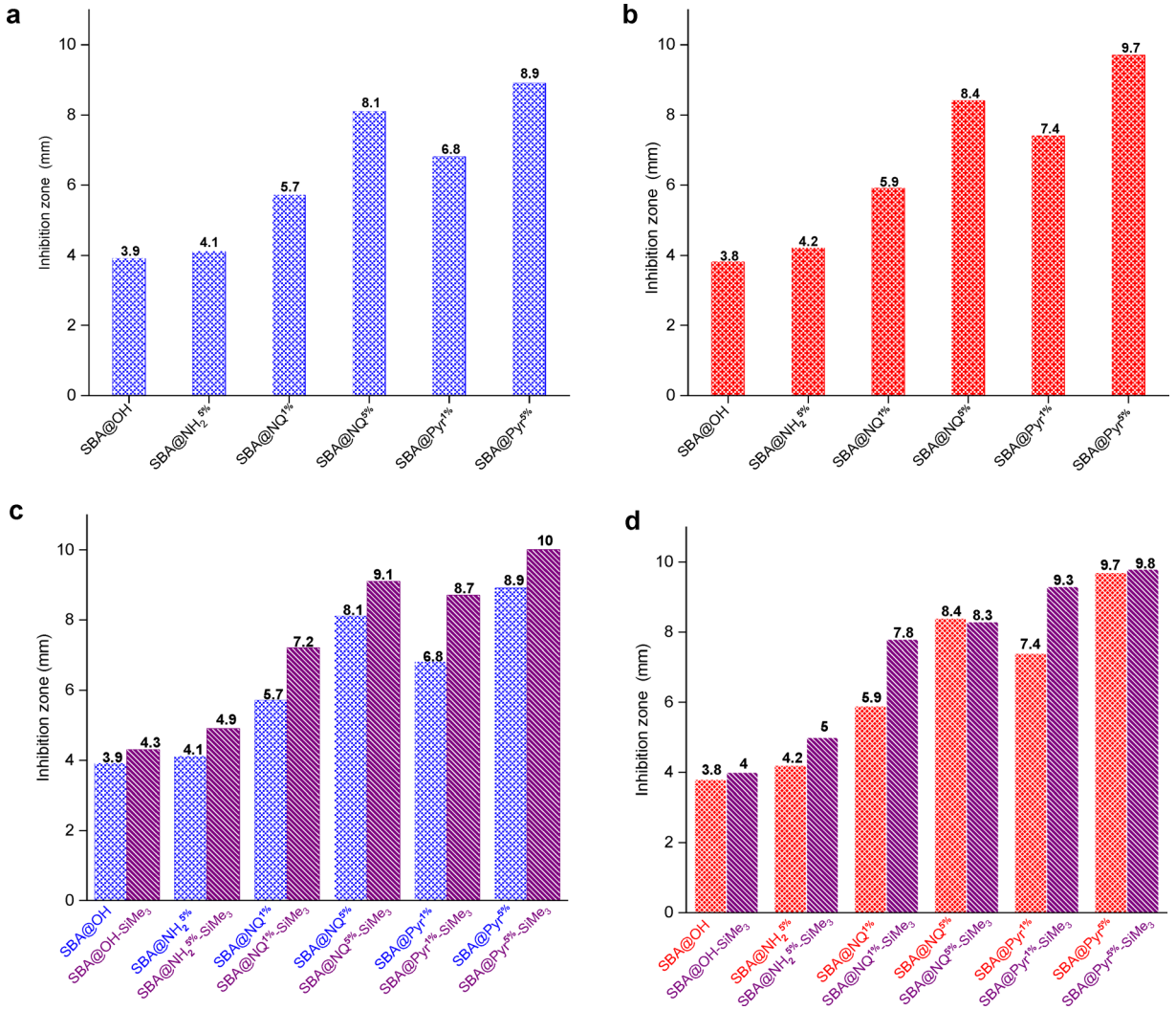

Fig. 6 Antibacterial activity of nitrogen-containing SBA-15 materials. (a) Performance of different materials for inhibiting the growth of Gram-negative *Escherichia coli*. (b) Performance of different materials for inhibiting the growth of Gram-positive *Staphylococcus aureus*. (c) Inhibition performance of non-passivated *versus* trimethylsilylated materials against Gram-negative *Escherichia coli*. (d) Inhibition performance of non-passivated *versus* trimethylsilylated materials against Gram-positive negative *Staphylococcus aureus*. 20 mg of the sample was compacted into a circular disc of 2 mm in diameter. The bacterial density is 1.5×10^6 CFU mL^{-1}. After 24 h at 37 °C, the diameter of the inhibition zones was measured (see the Experimental section for further details).

for the inhibition of *Escherichia coli*. The increase in the two cases of the inhibitory effect depending on the content of the nitrogen-containing groups clearly indicates their involvement in the biological activity. Comparing the performance of **SBA@NH$_2$$^{5\%}$** and the one of **SBA@NQ$^{1\%}$** reveals the superior inhibitory effect caused by ammonium compared to amine functionalities, although the nitrogen content of the former is more than three times superior to the content of the later. At nearly similar nitrogen loading, the inhibitory effect of ammonium is doubled compared to the primary amine, certainly because ammonium groups favor electrostatic interaction with bacteria, a preliminary step toward their destruction. The even greatest activity of **SBA@Pyr$^{X\%}$** also suggests the importance of the pyridinium–pyridine motif that outperforms the performance recorded for aliphatic ammonium groups of **SBA@NQ$^{X\%}$**. The involvement of the exposed pyridine, solely or in combination with the fused pyridinium, seems to be the most plausible mechanism, as the selective accessibility of the buried quaternary pyridinium has been challenged by the methyl orange adsorption test, as it has been discussed early.

To further investigate the importance of the surface polarity for eradicating bacterial cells, we further used the trimethylsilylated variants and benchmarked each sample with its non-passivated partner. The results clearly point to the positive effect imparted by the presence of trimethylsilyl groups, although this post-grating has been found to severely reduce the specific surface areas and could indeed be expected to limit access to the mesopores. At the same amount of the tether, the passivated material outperforms the non-passivated ones. Noteworthy is the activity reached with only 1% amount that has been next passivated, being higher that the inhibitory effect reached by introducing 5% leading. However, a steady-state was reached at 5% loading for the inhibition of *Staphylococcus aureus*, with the trimethylsilylation route being less effective to further boost the antibacterial performance. This result could be due to the marginal effect of the trimethylsilylation against **SBA@NQ$^{5\%}$**, which at this loading display already a C_{BET} value of 50, indicative of its pronounced hydrophobicity (Fig. 6c and d). In fact, at such loading, the vertical branching allows dimethylammonium to be much more close to each other while the remaining octadeyl behaves as a brush, exalting more pronounced hydrophobicity. In the case of **SBA@Pyr$^{5\%}$-SiMe$_3$**, while no variation in C_{BET} was observed, the most plausible explanation could be rooted in the reduced specific surface area of the corresponding material, being less favorable to the penetration of heavy objects like bacteria. Mechanistically speaking, bacteria could be drawn to the pores through electrostatic interactions. The positively charged ammonium in **NQSi** or pyridine pyridinium in **PyrSi** tethers strongly interacts with the negatively charged bacterial cell membranes, thereby facilitating its adhesion to the silica surface. Once within the pores, these interactions not only promoted bacterial attachment but also positioned the cells in close proximity to the antimicrobial functional groups. The hydrophobic backbone of the functionalized silica penetrated the bacterial peptidoglycan layer, which forms part of the cell wall. This penetration disrupted the integrity of the peptidoglycan network, compromising the cell wall's structural stability. As a result, the bacterial cell membrane became destabilized, leading to a loss of essential cellular components and ultimately causing cell lysis. This disruption of the cell walls and membrane integrity was the primary mechanism that led to bacterial death, as the cells were no longer able to maintain their osmotic balance or defend against external stressors. The improved antibacterial activity observed herein is in agreement with the enhanced bioactivity of the silica surface upon coating with fatty acids, attributed to the full coverage of the pristine silica surface.[43,44] The dependence of activity on both cationic charge density and hydrophobicity supports this proposed mechanism,[45–47] but further experiments are necessary to further clarify the biological action. In the whole, the improvement of the antibacterial activity of 1% loading after trimethylsilylation (**SBA@NQ$^{1\%}$-SiMe$_3$** and **SBA@Pyr$^{1\%}$-SiMe$_3$**) is one of the most selling points of these materials. Considering the wide availability of the passivating reagents and their cost-effectiveness compared to the cost of the starting precursors, more scalable materials could be designed by trivial tuning of their surface polarity.

Uptake and release of quercetin

In this part, we have selected only three nitrogen-containing organosilica to study their uptake, release and the anti-oxidant activity once entrapping quercetin. The ability of mesostructured silica to host active pharmaceuticals has been already demonstrated and further explored for designing controlled-release systems.[48] However, more research should be done to further explore the combination of synergistic action ''*per se* and loaded pharmaceutical''.[49] At a pH of 5.5, conventional **SBA@NH$_2$$^{5\%}$** achieves a lower uptake of 6%, while **SBA@Pyr$^{5\%}$** and **SBA@NQ$^{5\%}$** were able to host 16% and 20% of the quercetin drug, respectively. This trend perfectly concordats with the accessibility test as previously discussed (Fig. 7). A maximum adsorption capacity of 45 mg g^{-1}, corresponding to an efficient removal of 30% uptake, was rather observed for **SBA@OH**, thereby highlighting the occurrence of hydrogen bonding between Si–OH of the host and polar groups of the pharmaceutical. At a pH of 9.5, all the materials display an enhanced uptake of the pharmaceutical, with **SBA@NQ$^{5\%}$**, recording the highest value (75%) efficiency, with an adsorption capacity of 114 mg g^{-1} (Fig. 7). This spectacular uptake is due to the formation of anionic phenolate species upon quercetin deprotonation at pH $>$ 7.5, favoring cationic–anionic exchange between the positively charged **SBA@NQ$^{5\%}$** and its guest. **SBA@Pyr$^{5\%}$** and **SBA@NQ$^{5\%}$** loaded at pH = 5.5 trigger quercetin release, with **SBA@Pyr$^{5\%}$** enabling to escape more pharmaceutical (20%) compared to 11% release in the case of **SBA@NQ$^{5\%}$** (Fig. S11). This indicates that the loaded quercetin probably interacts through different ways with its adsorbent, with presumably less interactions occurring within the pores of **SBA@Pyr$^{5\%}$** compared to tighter interplay in the case of **SBA@NQ$^{5\%}$**. **SBA@NH$_2$$^{5\%}$** failed to release even a trace amount of the drug and consequently did not show any measurable

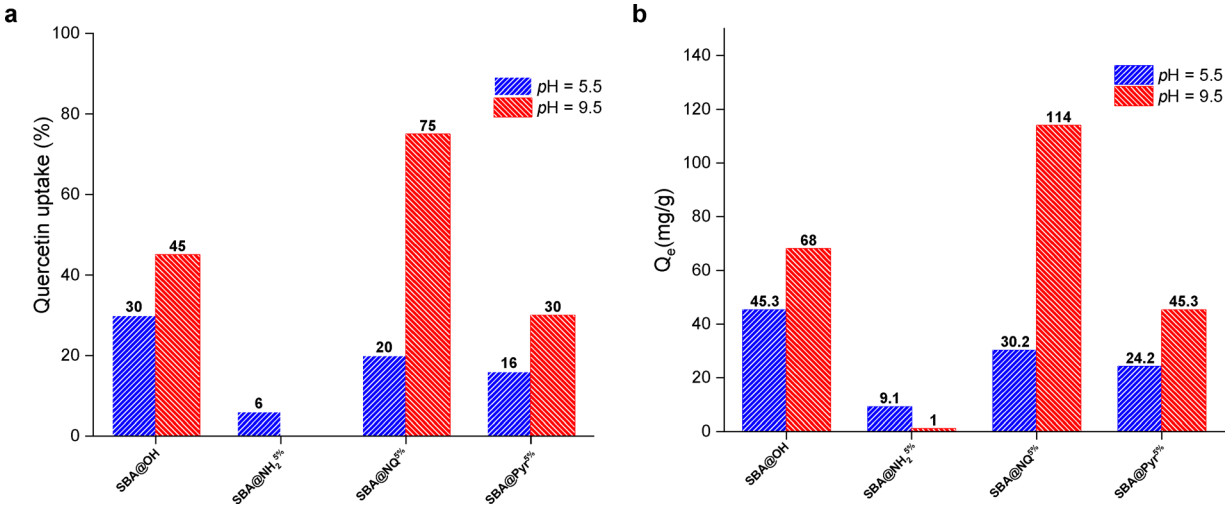

Fig. 7 Removal of quercetin using silica and the modified silica surface. (a) Percentage of quercetin removal, and (b) adsorption capacity on organosilicas at different pH values.

antioxidant activity. In contrast, **SBA@NQ$^{5\%}$_Q** and **SBA@Pyr$^{5\%}$_Q** display great antioxidant activity, with IC_{50} values of 0.7 and 0.48, respectively. These preliminary results demonstrate that these materials act synergistically as active antibacterial drugs and also as a reservoir for controlled release of antioxidants.

Experimental section

Starting reagents

Commercially available reagents and solvents were purchased from Across and Sigma-Aldrich and used without further purification. 3-(Trihydroxysilyl)propyldimethyloctadecyl ammonium (CAS number 27668-52-6) was purchased from across with 5% of purity in water.

Methods and materials

Fourier transform infrared (FTIR) spectra were obtained with a PerkinElmer Spectrum 100FT-IR spectrometer equipped with ATR accessory. The FTIR spectra were recorded in the 4000–600 cm^{-1} range with a resolution of 4 cm^{-1} and an accumulation of 32 scans. Solid-state ^{13}C CP-MAS NMR and ^{29}Si NMR spectra were recorded using a JEOL JNM-ECZR 600 MHz spectrometer, operating at 150 MHz for ^{13}C and 243 MHz for ^{29}Si. Cross-polarization (CP) was optimized individually for each sample to enhance signal sensitivity. Samples were packed into 3.2 mm zirconia rotors and spun at a magic angle spinning (MAS) speed of 22 kHz to reduce dipolar broadening and improve spectral resolution. The recycling delay was optimized based on the T_1 relaxation time for each sample to ensure efficient signal recovery between scans. For the ^{13}C CP-MAS NMR spectra, a ramped CP sequence was employed with high-power proton decoupling during acquisition. The contact time was individually optimized for each sample. Additionally, high-resolution ^{1}H NMR and 2D ^{1}H homocorrelation spectra were acquired to address the limitations in sensitivity for ^{13}C and ^{29}Si, taking advantage of the enhanced resolution achieved with a higher MAS speed of 22 kHz. All spectra were processed using standard methods, including Fourier transformation, baseline correction, and line broadening, to enhance resolution and signal clarity. Diffuse reflectance UV-visible spectroscopy (DRUV) was measured in the 200–800 nm wavelength range using a PerkinElmer Lambda 1050 spectrometer equipped with an integrating sphere. Thermogravimetric analysis (TGA) was performed using a Discovery TGA analyzer at a heating rate of 15 °C min^{-1} from room temperature to 600 °C under a nitrogen atmosphere. Textural properties were evaluated through nitrogen adsorption–desorption isotherms using a TriStar II Plus (Micromeritics) analyzer. Measurements were conducted at 77.3 K following a degassing step at 120 °C for 12 hours to eliminate surface moisture and physisorbed species. The specific surface area was calculated using the Brunauer–Emmett–Teller (BET) method. SEM images were obtained using a JEOL JSM 6700F. Energy dispersive X-ray spectroscopy (EDS-SEM) analyses of the powders were performed using an Oxford EDS system. TEM images were obtained using a JEOL JEM 2010 at an activation voltage of 200 kV. We tested the antibacterial properties of organosilica by using a total viable colony count method.[50] The study focused on two foodborne pathogens, namely *Escherichia coli* (Gram-negative) and *Staphylococcus aureus* (Gram-positive). For the experiment, the bacterial strains were aseptically cultured in 20 mL of tryptic soy broth (TSB) for *E. coli* and brain heart infusion (BHI) broth for *S. aureus*. The cultures were incubated at 37 °C for 16 hours. After incubation, the bacterial suspension was diluted to a concentration of 10^5–10^6 CFU mL^{-1}, and 20 mL of the diluted suspension was transferred into a 100 mL conical flask containing 100 mg of the film sample. The flask was incubated at 37 °C with gentle shaking for 12 hours. A control flask containing only the diluted broth (without the film) was also included. Viable bacterial counts (expressed as Log10 CFU mL^{-1}) were recorded at 2, 4, 8, and 10-hour intervals by plating the samples onto

agar plates. Each measurement was performed in triplicate at each time point to ensure accuracy.

Preparation of 1-(3-trimethoxysilylpropyl)-4-(4-pyridyl)pyridinium bromide

An equimolar amount of the commercially available 4,4′-bipyridine (500 mg, 3.2 mmol) reacted with 3-iodopropyltrimethoxysilane (1 mL, 4.8 mmol) in 10 mL of acetonitrile for 24 h at room temperature. The temperature was then increased to 85 °C and the reaction mixture was stirred for an additional 24 hours. The obtained orange solid was subjected to filtration and washed three times with 10 mL of toluene. Ionic exchange of an iodide ion by bromide was done through using 10 mL of HBr in water (4 M). The mixture was then filtered and washed twice with 5 mL of HBr (4 M), followed by drying at 80 °C for 4 hours.

Preparation of pristine and nitrogen-containing SBA-15-type organosilica

SBA@OH. 2 g of the Pluronic P123 was stirred in an acidic solution (15 mL of water and 60 mL of HCl (2 M)) for 2 hours at 35 °C. Then, 4.5 mL (0.02 mol) of TEOS was added to the reaction mixture, which was subsequently stirred for 24 hours. Temperature was then gradually increased to 80 °C and maintained for 48 hours. The Pluronic was removed by Soxhlet extraction using 200 mL of ethanol acidified with 5 mL of hydrochloric acid (37%). The process was conducted over a continuous period of 96 hours to ensure exhaustive extraction. 2 g of the resulting white powder was collected after drying at 80 °C during 12 h.

SBA@OH-SiMe$_3$. To 100 mg of **SBA@OH** suspended in 5 mL of toluene, we added 0.2 mL of HMDS and stirred the mixture at room temperature for 24 hours. The resulting powder was next isolated through filtration (toluene 5 mL × 3 and one time with 3 mL of acetone). 82 mg of the resulting white powder was collected after drying at 80 °C during 12 h.

SBA@NH$_2$$^{5\%}$. 2 g of the Pluronic P123 was stirred in an acidic solution (15 mL of water and 60 mL of HCl (2 M)) for 2 hours at 35 °C. Then, 0.02 mol of TEOS and 0.1 mmol of **APTES** (5% relative to TEOS) were simultaneously added to the mixture and stirred for 24 hours. Subsequently, the temperature was gradually increased to 80 °C and maintained for 48 hours. Pluronic P123 was then removed by Soxhlet extraction using 200 mL of ethanol acidified with 5 mL of hydrochloric acid (37%). The extraction was carried out continuously over 96 hours to ensure complete removal. After drying at 80 °C for 12 hours, 1.8 g of the resulting white powder was collected.

SBA@NH$_2$$^{5\%}$-SiMe$_3$. To 100 mg of **SBA@NH$_2$$^{5\%}$** dispersed in 5 mL of toluene, we added 0.2 mL of HMDS and stirred the mixture at room temperature for 24 hours. Then, the resulting powder was isolated through filtration (three times with 5 mL of toluene and another one with 3 mL of acetone). 90 mg of the white powder denoted as **SBA@NH$_2$$^{5\%}$-SiMe$_3$** was collected after drying at 80 °C during 12 h.

SBA@NQ$^{X\%}$(*X* = 1 or 5). 2 g of the Pluronic P123 was stirred in an acidic solution (15 mL of water and 60 mL of HCl (2 M)) for 2 hours at 35 °C. Then, 0.02 mol of TEOS and a given amount of **NQSi** (0.2 mmol corresponding to 1% and 1 mmol corresponding to 5% TEOS) were simultaneously added to the mixture and stirred for 24 hours. Subsequently, the temperature was gradually increased to 80 °C and maintained at that level for 48 hours. Removal of the Pluronic was done through Soxhlet extraction using 200 mL of ethanol acidified with 5 mL of hydrochloric acid (37%) for 96 hours. 1.7 g of the resulting white powder was collected after drying at 80 °C during 12 h.

SBA@NQ$^{X\%}$-SiMe$_3$ (*X* = 1 or 5). To 300 mg of **SBA@NQ$^{X\%}$** (*X* = 1 or 5) suspended in 5 mL of toluene, we added 0.2 mL of HMDS and stirred the mixture at room temperature for 24 hours. Then, the resulting powder was isolated through filtration and washed three times with toluene 5 mL and next with 3 mL of acetone. 310 mg of the resulting white powder was collected after drying at 80 °C during 12 h.

SBA@Pyr$^{X\%}$ (*X* = 1 or 5). 2 g of the Pluronic P123 was stirred in an acidic solution (15 mL of deionized water and 60 mL of HCl (2 M)) for 2 hours at 35 °C. Then, TEOS (0.02 mol) and **PyrSi** (8 mg, 0.2 mmol corresponding to 1% and 40 mg, 1 mmol corresponding to 5% molar ratio of TEOS) were added to the mixture and stirred at room temperature for 24 hours. Subsequently, the temperature was gradually increased to 80 °C and maintained for 48 hours. Pluronic was removed by Soxhlet extraction using 200 mL of ethanol acidified with 5 mL of hydrochloric acid (37%) for 96 hours. After drying at 80 °C for 12 hours, 2 g of the resulting white powder was collected.

SBA@Pyr$^{X\%}$-SiMe$_3$. (*X* = 1 or 5). To 300 mg of **SBA@Pyr$^{X\%}$** suspended in 5 mL of toluene, we added 0.2 mL of HMDS and left the mixture for stirring at room temperature for 24 hours. Then, the resulting powder was isolated through filtration, washed three times with 5 mL of toluene and next with 3 mL of acetone. 270 mg of the resulting white powder was collected after drying at 80 °C for 12 h.

SBA@BPyr$^{5\%}$. To 150 mg of **SBA@Pyr$^{5\%}$**, 3 mL of methyl iodide was added, and the mixture was refluxed in 5 mL DMF for 72 hours. The resulting powder was next treated in Soxhlet, using 100 mL dichloromethane/diethylic ether (1/1). The extraction process was conducted over a continuous period of 2 hours. 120 mg of the resulting white powder was collected after drying at 80 °C for 12 h.

SBA@BPyr$^{5\%}$-SiMe$_3$. To 75 mg of **SBA@BPyr$^{5\%}$** suspended in 5 mL of toluene, we added 0.5 mL of HMDS and the mixture was stirred for 24 h at room temperature. After filtration and washing three times with 5 mL of toluene and next with 3 mL of acetone, 80 mg of the resulting white powder was collected after drying at 80 °C for 12 h.

Quercetin loading. 10 mg of organosilica was dispersed in 5 mL of quercetin ($C = 10^{-3}$ M) in ethanol. Next, the resulting mixture was gently stirred for 6 hours. The resulting solid was then filtered, washed with water and dried at 80 °C overnight.[51] The resulting quercetin loaded silica materials were labelled **SBA@NQ$^{5\%}$_Q** and **SBA@Pyr$^{5\%}$_Q**.

Quercetin release. Quercetin release study was performed in water/ethanol 1 : 1 at a pH of 5.5 through dispersing **SBA@NQ$^{5\%}$_Q** and **SBA@Pyr$^{5\%}$_Q** at C_m = 2 mg mL^{-1}.

The released quercetin was calculated using an UV-vis spectrophotometer by monitoring the intensity change of the adsorption bond at λ = 367 nm.[51]

Antioxidant activity. After quercetin release in water/ethanol (1/1) (C_m = 2 mg mL^{-1}), three successive dilutions were prepared (1 mg mL^{-1}, 0.5 mg mL^{-1} and 0.25 mg mL^{-1}) to evaluate their antioxidant activity *via* DPPH assay. The DPPH concentration was calculated using an UV-vis spectrophotometer at 517 nm.[52]

Helianthine adsorption. 10 mg of organosilicas were dispersed in 5 mL of an aqueous solution of methyl orange (10^{-4} M) and stirred at room temperature for 6 hours. The adsorption process was monitored by UV-vis spectroscopy by measuring the decrease in absorbance at λ = 463 nm at pH= 6.5 and 9.5 and at λ = 505 nm at pH = 2. The pH is adjusted using HCl (0.1 M) and NaOH (0.1 M).

Antibacterial activity

The disc diffusion method was chosen to study the antibacterial activity of organosilica powder against Gram-positive (*Staphylococcus aureus*) and Gram-negative (*Escherichia coli*) bacteria. The powders were compacted into a circular disc of 2 mm in diameter. After sterilization, the circles were spread on the Mueller Hinton agar surface using a bacterial density of approximately 1.5 × 10^6 CFU mL^{-1}. The samples were kept for 24 h at 37 °C and the diameters of the inhibition zones around the circles were measured.

Conclusions

With the sake of designing more powerful, metal-free, antibacterial materials, we have herein designed a set of nitrogen-containing SBA-15-type mesoporous materials. Pyridyl-pyridinium and dodecylammonium were successfully embedded within the material framework, without disrupting the mesostructure ordering. The effect of the tether amount (1% *versus* 5%) was investigated and proved to be pivotal for inhibiting the bacterial growth. Interestingly, substantial amplification was also observed by trivial switching the silica surface polarity from hydrophilic to hydrophobic through trimethylsilylation. This surface functionalization provides a way for improving the antibacterial performance while minimizing the amount of the costly active ingredient used. Besides, nitrogen functionalities offer an additional role of interacting with entrapped drugs as exemplified by the uptake and release of antioxidant-based pharmaceuticals. With the well-established versatility of mesoporous materials and the wealth of available precursors, surface-chemistry opens new channels of possibilities for the design of cost-effective metal-free antiviral and antibacterial materials, with expanded possibilities towards multifunctional and synergistic drug transporters.

Conflicts of interest

There are no conflicts to declare.

Data availability

Data are available in the supplementary information (SI). Supplementary information is available. See DOI: **https://doi.org/10.1039/d5ma00714c**.

Acknowledgements

Hassan II academy of Science and Technology is acknowledged for the financial support from the Nano-Bio-Mat project.

Notes and references

1 A. C. Kresge, M. E. Leonowicz, W. J. Roth, J. Vartuli and J. Beck, *Nature*, 1992, **359**, 710–712.
2 H.-P. Lin and C.-Y. Mou, *Science*, 1996, **273**, 765–768.
3 D. Zhao, Q. Huo, J. Feng, B. F. Chmelka and G. D. Stucky, *J. Am. Chem. Soc.*, 1998, **120**, 6024–6036.
4 D. Zhao, J. Feng, Q. Huo, N. Melosh, G. H. Fredrickson, B. F. Chmelka and G. D. Stucky, *Science*, 1998, **279**, 548–552.
5 J. S. Beck, J. C. Vartuli, W. J. Roth, M. E. Leonowicz, C. T. Kresge, K. D. Schmitt, C. T. Chu, D. H. Olson, E. W. Sheppard and S. B. McCullen, *J. Am. Chem. Soc.*, 1992, **114**, 10834–10843.
6 B. L. Newalkar, N. V. Choudary, P. Kumar, S. Komarneni and T. S. G. Bhat, *Chem. Mater.*, 2002, **14**, 304–309.
7 L. Paul, S. Mukherjee, S. Chatterjee, A. Bhaumik and D. Das, *ACS Omega*, 2019, **4**, 17857–17863.
8 P. Verma, Y. Kuwahara, K. Mori, R. Raja and H. Yamashita, *Nanoscale*, 2020, **12**, 11333–11363.
9 V. Mamaeva, C. Sahlgren and M. Lindén, *Adv. Drug Delivery Rev.*, 2013, **65**, 689–702.
10 A. Bernardos, E. Piacenza, F. Sancenon, M. Hamidi, A. Maleki, R. J. Turner and R. Martínez-Máñez, *Small*, 2019, **15**, 1900669.
11 Y. Song, H. Jiang, B. Wang, Y. Kong and J. Chen, *ACS Appl. Mater. Interfaces*, 2018, **10**, 1792–1801.
12 M. Sanchez-Milla, R. Gomez, J. Perez-Serrano, J. Sanchez-Nieves and F. J. de la Mata, *Mater. Sci. Eng., C*, 2020, **109**, 110526.
13 J. Zhang, W. Guo, Q. Li, Z. Wang and S. Liu, *Environ. Sci.: Nano*, 2018, **5**, 2482–2499.
14 M. Sharifi, M. K. Farahani, M. Salehi, A. Atashi, M. Alizadeh, R. Kheradmandi and S. Molzemi, *ACS Biomater. Sci. Eng.*, 2022, **9**, 106–138.
15 A. F. Fakhardo, E. I. Anastasova, S. R. Gabdullina, A. S. Solovyeva, V. B. Saparova, V. V. Chrishtop, E. D. Koshevaya, E. F. Krivoshapkina, P. V. Krivoshapkin and G. O. Kiselev, *ACS Appl. Bio. Mater.*, 2019, **2**, 4427–4435.
16 L. Chen, S. Zhang, Y. Duan, X. Song, M. Chang, W. Feng and Y. Chen, *Chem. Soc. Rev.*, 2024, **53**, 1167–1315.
17 A. Stein, B. J. Melde and R. C. Schroden, *Adv. Mater.*, 2000, **12**, 1403–1419.
18 J. M. Rosenholm and M. Lindén, *Chem. Mater.*, 2007, **19**, 5023–5034.

19 S. Fiorilli, B. Onida, B. Bonelli and E. Garrone, *J. Phys. Chem. B*, 2005, **109**, 16725–16729.
20 S. Rahmani, K. Bouchmella, J. Budimir, L. Raehm, M. B. Cardoso, P. Trens, J.-O. Durand and C. Charnay, *ACS Omega*, 2019, **4**, 1479–1486.
21 M. Álvaro, B. Ferrer, V. Fornés and H. García, *Chem. Commun.*, 2001, 2546–2547.
22 N. Fattori, C. M. Maroneze, H. A. Magosso, Y. V. Kholin and Y. Gushikem, *J. Colloid Interface Sci.*, 2012, **384**, 137–142.
23 Y. Zhu, H. Li, Q. Zheng, J. Xu and X. Li, *Langmuir*, 2012, **28**, 7843–7850.
24 F. Sevimli and A. Yılmaz, *Microporous Mesoporous Mater.*, 2012, **158**, 281–291.
25 M. Thanigachalam and A. V. M. Subramanian, *Biomater Transl.*, 2023, **4**, 151.
26 H. Guo, M. Guo, Z. Xia and Z. Shao, *Biomater Transl.*, 2024, **5**, 33.
27 W. Ma, H. Lu, Y. Xiao and C. Wu, *Org. Res.*, 2025, **1**, 025040004.
28 N. Prabhakar, E. Långbacka, E. Özliseli, J. Mattsson, A. Mahran, I. Suleymanova, C. Sahlgren, J. M. Rosenholm, M. Åkerfelt and M. Nees, *Small Sci.*, 2024, **4**, 2400084.
29 M. Michailidis, I. Sorzabal-Bellido, E. A. Adamidou, Y. A. Diaz-Fernandez, J. Aveyard, R. Wengier, D. Grigoriev, R. Raval, Y. Benayahu and R. A. D'Sa, *ACS Appl. Mater. Interfaces*, 2017, **9**, 38364–38372.
30 J. Huang, R. R. Koepsel, H. Murata, W. Wu, S. B. Lee, T. Kowalewski, A. J. Russell and K. Matyjaszewski, *Langmuir*, 2008, **24**, 6785–6795.
31 B. Gottenbos, H. C. van der Mei, F. Klatter, P. Nieuwenhuis and H. J. Busscher, *Biomaterials*, 2002, **23**, 1417–1423.
32 Z. Li, D. Lee, X. Sheng, R. E. Cohen and M. F. Rubner, *Langmuir*, 2006, **22**, 9820–9823.
33 J. J. Oosterhof, K. J. Buijssen, H. J. Busscher, B. F. van der Laan and H. C. van der Mei, *Appl. Environ. Microbiol.*, 2006, **72**, 3673–3677.
34 J. Song, H. Kong and J. Jang, *Colloids Surf., B*, 2011, **82**, 651–656.
35 K. Kuciński and G. Hreczycho, *ChemSusChem*, 2019, **12**, 1043–1048.
36 S. G. de Ávila, L. C. C. Silva and J. R. Matos, *Microporous Mesoporous Mater.*, 2016, **234**, 277–286.
37 J. D. Webb, T. Seki, J. F. Goldston, M. Pruski and C. M. Crudden, *Microporous Mesoporous Mater.*, 2015, **203**, 123–131.
38 J. C. Markwart, A. Battig, M. M. Velencoso, D. Pollok, B. Schartel and F. R. Wurm, *Molecules*, 2019, **24**, 3901.
39 A. El Kadib, N. Katir, A. Finiels, A. Castel, N. Marcotte, K. Molvinger, C. Biolley, P. Gaveau, M. Bousmina and D. Brunel, *Dalton Trans.*, 2013, **42**, 1591–1602.
40 A. El Kadib, P. Hesemann, K. Molvinger, J. Brandner, C. Biolley, P. Gaveau, J. J. Moreau and D. Brunel, *J. Am. Chem. Soc.*, 2009, **131**, 2882–2892.
41 Y. Brahmi, N. Katir, A. Castel and A. El Kadib, *Microporous Mesoporous Mater.*, 2013, **177**, 75–81.
42 M. Ferenc, N. Katir, K. Miłowska, M. Bousmina, J.-P. Majoral, M. Bryszewska and A. El Kadib, *J. Mater. Chem. B*, 2015, **3**, 2714–2724.
43 E. Pędziwiatr-Werbicka, K. Miłowska, M. Podlas, M. Marcinkowska, M. Ferenc, Y. Brahmi, N. Katir, J. P. Majoral, A. Felczak and A. Boruszewska, *Chem. – Eur. J.*, 2014, **20**, 9596–9606.
44 M. Ferenc, N. Katir, K. Milowska, M. Bousmina, Y. Brahmi, A. Felczak, K. Lisowska, M. Bryszewska and A. El Kadib, *Micropor. Mesopor. Mat*, 2016, **231**, 47–56.
45 K. Ciepluch, N. Katir, A. El Kadib, A. Felczak, K. Zawadzka, M. Weber, B. Klajnert, K. Lisowska, A.-M. Caminade and M. Bousmina, *Mol. Pharm.*, 2012, **9**, 448–457.
46 N. Katir, J. P. Majoral, A. El Kadib, A.-M. Caminade and M. Bousmina, *Eur. J. Org. Chem.*, 2012, 269–273.
47 M. Boundor, B. Bielska, N. Katir, N. Wronska, K. Lisowska, M. Bryszewska, K. Miłowska and A. El Kadib, *ACS Appl. Polym. Mater.*, 2023, **5**, 9952–9963.
48 M. Vallet-Regi and A. Ramila, *Chem. Mater.*, 2001, **13**, 308–311.
49 M. Cokol, H. N. Chua, M. Tasan, B. Mutlu, Z. B. Weinstein, Y. Suzuki, M. E. Nergiz, M. Costanzo, A. Baryshnikova and G. Giaever, *Mol. Syst. Biol.*, 2011, **7**, 544.
50 J.-W. Liu, T. Fu, Y. He, L.-J. Wang, K.-R. Ding and H.-Z. Zhao, *Chem. Eng. J.*, 2024, **497**, 154770.
51 I. Trendafilova, A. Szegedi, J. Mihály, G. Momekov, N. Lihareva and M. Popova, *Mater. Sci. Eng., C*, 2017, **73**, 285–292.
52 O. P. Sharma and T. K. Bhat, *Food Chem.*, 2009, **113**, 1202–1205.